

The role of solute diffusion in dynamical evolution during directional solidification: From a viewpoint of dissipation

Fengyi Yu

CAS Key Laboratory of Mechanical Behavior and Design of Materials, Department of Modern Mechanics,

University of Science and Technology of China, Hefei 230026, China

E-mail address: fengyi.yu.90@gmail.com

Abstract

The theoretical insights of dynamics most focus on one single dendrite tip at different stages of directional solidification. Through the phase-field model, this paper investigates the evolution in the whole domain during entire directional solidification. Firstly, the evolution of characteristic parameters is obtained, including the solute concentration ahead of interface and tip velocity, demonstrating the dissipative features of solidification. Secondly, by adjusting the diffusion coefficient D_L , the dissipation at the interface can be altered. With different D_L , different stages during directional solidification are investigated, including planar growth and instability, dendrite growth, and steady-state growth. From the viewpoint of dissipation, the role of solute diffusion in evolution is given out. Even under the local equilibrium conditions, the dissipation at the interface plays an important role in alloy solidification, altered by solute diffusion. Moreover, the competitive influences of tip curvature and velocity are also because of the dissipation.

Keywords

Diffusion; Directional solidification; Dissipative.

Introduction

The mechanical properties of as-solidified components are dominated by solidification structures. The precise control of the structures requires a deep understanding of solidification dynamics. The dynamics is determined by the competition between the transport of heat and mass and the inherent length scale of the material induced by interfacial energy.^{1,2} In this spirit, considerable achievements have been made, including theoretical models, numerical simulations, and the corresponding experimental observations.³⁻⁵

Due to its complexity, researchers developed various theoretical models to describe the evolution at different solidification stages, separately. For early-stage growth, including the planar growth and instability, the descriptions go through the Constitutional Supercooling (CS) theory,⁶ Mullins-Sekerka (MS) analysis,⁷ to the Warren-Langer (WL)⁸ model. The WL model represents the interplay of the time-dependent transport and interfacial processes. The incubation time and average wavelength of planar instability predicted by the WL model consist of the experimental observations.^{9,10} After the planar instability, solidification turns into dendrite growth (with or without sidebranches). In dendrite growth, two stages are distinguished due to the different features. The first is the unsteady growth; the velocity and shape of the dendrite tip vary with time. The second is the steady-state growth; the velocity and shape are constant. The competitive influences of the tip radius ρ and velocity V_I determine the dendrite growth.^{11,12} Up to now, a number of theoretical insights have been presented, expressing the relations between the dynamical evolution and characteristic parameters ρ and V_I . However, the solutions of the theoretical models can only apply under simple conditions. Hence, the theoretical insights mostly focus on one single dendrite tip (local), ignoring the transport in the global system. Moreover, the separate descriptions at different stages mean the loss of continuity of the evolution, which could hardly represent the history-dependence of solidification.

Differing from theoretical models, numerical models have the advantage of handling complicated interfacial morphologies and varying solidification parameters.^{13,14} As one of them, the Phase-Field (PF) method has solid physical foundations and high numerical accuracy.¹⁵⁻¹⁷ Physics underlying the construction of the PF model includes insights from thermodynamics and dynamics of the transport, as well as the interfacial anisotropy.^{18,19} When solving the governing equations, using an additional scalar field to implicitly represent the interface by one of its level sets, the PF method avoids the shape error caused by tracking interface. It can capture complex interfacial morphologies and characteristic parameters at the interface with high accuracy. With the significant advantages, the PF method has been increasingly applied

to investigating solidification dynamics, including the planar to cellular transition,^{20, 21} the selection of growth direction,^{22, 23} and the sidebranching dynamics^{24, 25}, etc. The consistencies with the experimental observations demonstrate the accuracy of the PF method.

However, the existing analyses lack insights of historical relevance and transport processes in the whole system. On the one hand, the local equilibrium does not mean the whole system is at equilibrium. The gradients of temperature and concentration are present. On the other hand, for macroscopic phenomena, the microscopic particles are too many to focus on separately. The system in the studies is regarded as an open system. Through exchanging heat and mass with the environment, solidification structures are formed out of equilibrium in an open system, i.e., a dissipative system.²⁶ Unlike equilibrium systems, dissipative systems develop patterns or structures they do not have when first formed. The initial evolution can be deterministic for subsequent evolution. That is, solidification is a history-dependent process. The investigation during the entire process and the insights from dissipation can provide new perspectives on solidification dynamics.

Through the quantitative PF model, this paper investigates the evolution in the whole domain during entire directional solidification. Firstly, the evolution of the characteristic parameters is discussed in detail, showing the dissipative features. Secondly, by adjusting the diffusion coefficient D_L , the dissipation of the system can be altered. With different D_L , different stages during directional solidification are investigated, including planar growth and instability, dendrite growth, and steady-state growth. From the viewpoint of dissipation, the role of solute diffusion in alloy solidification is given out.

Models and methodology

For directional solidification, the so-called “frozen temperature approximation” is adopted:

$$T(z,t) = T_0 + G \left(z - \int V_p(t) dt \right) \quad (1)$$

where T_0 is the melt temperature of the pure material, G is the thermal gradient, and V_p is the pulling speed. The approximation is based on the assumptions: (1) The latent heat is ignored, i.e., the temperature field is undisturbed by the evolution of the Solid/Liquid (S/L) interface. It is essentially a statement concerning the relative magnitudes of the terms in the Stefan condition, $\rho_s L_f v^* n \ll k_{s,l} \nabla T_{s,l} \cdot n$.²⁷ In the expression, ρ_s is the density of the solid, L_f is the latent heat, and $v^* n$ is the rate of solidification. $k_{s,l}$ is the thermal conductivity, $\nabla T_{s,l}$ is the thermal gradient, and n is the normal direction of the interface. The rate of alloy solidification ($v^* n$) is limited by solute diffusion. Since the coefficient of thermal conductivity is much larger than solute

diffusion, the latent heat can be released quickly through heat conduction. Hence, the effect of the latent heat on thermal transport could be ignored.²⁸ (2) There is no flow in the liquid, consistent with the assumption that the densities of the solid and liquid are equal.

It should be noted, the frozen temperature approximation is just for heat transport. The solidification process contains the latent heat, both in the theoretical model and the PF model.

A. Theoretical model

The theoretical model is based on the linear instability analysis under non-steady-state conditions, the detailed derivations can be found in the literature 8, 29, 30. The following are the key equations.

The time-dependent concentration ahead of the interface c_0 , position of the interface z_0 , and diffusion length l can be expressed as:⁸

$$c_0(z_0, t) = \frac{2D_L c_\infty}{2D_L - V_I(1-k)l} \quad (2)$$

$$\frac{\partial z_0}{\partial t} = V_I - V_P(t) = \frac{2D_L(z_0 - z_\infty)}{l(1-k)z_0} - V_P(t) \quad (3)$$

$$\frac{\partial l}{\partial t} = \frac{4D_L(z_\infty - kz_0)}{l(1-k)z_0} - \frac{l}{z_0 - z_\infty} \frac{\partial z_0}{\partial t} \quad (4)$$

where D_L is the diffusion coefficient in the liquid, c_∞ is the average concentration, k is the solute partition coefficient, and V_I is the instantaneous velocity of the interface. z_∞ is the steady-state position of the planar interface with the relation of $z_\infty = -m \cdot c_\infty / G$, where G is the thermal gradient, and m is the slope of the liquidus line in the phase diagram.

Based on the time-dependent linear stability analysis and the assumption of an infinitesimal sinusoidal perturbation with spacing frequency ω , the increase rate of perturbation amplitude can be given by:

$$\sigma_\omega(t) = [dA_\omega(t)/dt] / A_\omega(t) \quad (5)$$

where $A_\omega(t)$ is the amplitude. Combining the interface position and diffusion length in [equations \(3\)-\(4\)](#), the dispersion relation of the perturbation under the transient conditions can be expressed by:³⁰

$$q_\omega \left\{ 1 + \frac{2[z_0(t) - z_\infty]}{l(t)} + \frac{\Gamma \omega^2}{G} \right\} = \frac{V_I(t) - V_P(t)}{D_l} + \frac{2[z_0(t) - z_\infty]}{l(t)} \cdot \left[\frac{V_I(t)}{D_l} + \frac{\sigma_\omega(t)}{V_I(t)} + \frac{1}{z_0(t)} + \frac{\Gamma \omega^2}{G \cdot z_0(t)} \right] \quad (6)$$

where q_ω is the inverse decay length of the concentration fluctuation at the interface along the z direction. Γ is the Gibbs-Thomson coefficient.

Based on equation (6), the time-dependent increase rate of the amplification rate $\sigma_\omega(t)$ can be obtained. Then according to the solution of equation (5), the time-dependent amplitude is:

$$A_\omega(t) = A_\omega(0) \exp \left[\int_{t_0}^t \sigma_\omega(t) dt \right] \quad (7)$$

where t_0 is the critical time when σ_ω changes from negative to positive. $A_\omega(0)$ refers to the initial amplitude of the infinitesimal fluctuation.

B. Phase-Field model

The following is a brief introduction to the quantitative PF model for alloy solidification. The driving force in this PF model is the difference in grand potential between phases.^{31, 32} The potential is related to the grand canonical ensemble of statistical mechanics, corresponding to an open system.³³

In the PF model, a scalar variable $\phi(\mathbf{r}, t)$ is introduced to identify the state of phase, where $\phi=+1$ reflects the solid, $\phi=-1$ reflects the liquid, and intermediate values of ϕ reflect the S/L interface. Since ϕ varies smoothly across the interface, the sharp interface becomes diffuse and the phases turn into a continuous field, i.e., phase field $\phi(\mathbf{r}, t)$. For alloy solidification, the solute field $c(\mathbf{r}, t)$ is represented by the supersaturation field $U(\mathbf{r}, t)$:

$$U = \frac{1}{1-k} \left(\frac{2kc/c_\infty}{1+k-(1-k)\cdot\phi} - 1 \right) \quad (8)$$

Combined with the frozen temperature approximation, the governing equations of the phase field and supersaturation field are given by equations (9)-(10):^{31, 34, 35}

$$\begin{aligned} a_s^2(\hat{n}) \left[1 - (1-k) \frac{z - \int V_p(t) dt}{l_T} \right] \frac{\partial \phi}{\partial t} = \\ \nabla \cdot [a_s^2(\hat{n}) \vec{\nabla} \phi] - \partial_x (a_s(\hat{n}) \cdot \vec{a}_s(\hat{n}) \cdot \partial_y \phi) + \partial_y (a_s(\hat{n}) \cdot \vec{a}_s(\hat{n}) \cdot \partial_x \phi) \\ + \phi(1-\phi^2) - \lambda(1-\phi^2)^2 \left[U + \frac{z - z_0 - \int V_p(t) dt}{l_T} \right] \end{aligned} \quad (9)$$

$$\left(\frac{1+k}{2} - \frac{1-k}{2} \phi \right) \frac{\partial U}{\partial t} = \nabla \cdot [D_L \cdot q(\phi) \cdot \vec{\nabla} U - \vec{j}_{at}] + \frac{1}{2} [1 + (1-k)U] \frac{\partial \phi}{\partial t} \quad (10)$$

where,

$$l_T = \frac{\Delta T_0}{G(t)} = \frac{|m| c_\infty (1-k)}{k G(t)} \quad (11)$$

$$a_s(\hat{n}) \equiv a_s(\theta + \theta_0) = 1 + \varepsilon_4 \cos 4(\theta + \theta_0) \quad (12)$$

$$q(\phi) = \frac{1-\phi}{2} \quad (13)$$

$$\vec{j}_{at} = -\frac{1}{2\sqrt{2}} [1 + (1-k)U] \frac{\partial \phi}{\partial t} \frac{\vec{\nabla} \phi}{|\vec{\nabla} \phi|} \quad (14)$$

In these equations, l_T means the thermal length, where m is the slope of the liquidus line in the phase diagram. $a_s(n)$ is the four-fold anisotropy function in a 2D system, where ε_4 is the anisotropy strength, θ is the angle between the normal direction of interface and the z-axis, and θ_0 is the intersection angle between the Preferred Crystallographic Orientation (PCO) of the crystal and the Thermal Gradient Direction (TGD) (here the TGD is parallel to the z-axis). $q(\phi)$ is an interpolation function determining the varying solute diffusion coefficient across the domain. \vec{j}_{at} is the Anti-Trapping Current (ATC) term, where $\partial\phi/\partial t$ means the rate of solidification, and $\nabla\phi/|\nabla\phi|$ is the unit length along the normal direction of the S/L interface.

It should be noted, [equation \(9\)](#) provides a clear connection between anisotropy of the microscopic and macroscopic levels. And it unifies the anisotropy in equilibrium and non-equilibrium conditions.^{18, 36} In [equation \(10\)](#), the ATC term counterbalances the trapping current associated with the jump of chemical potential across the interface and modifies the mass conservation condition at the interface. Specifically, the concentrations on both sides of the interface vary with velocity, they do not satisfy the partition relation (out of equilibrium). The jump of supersaturation can be interpreted as resulting from a finite interface mobility that leads to interface dissipation.³⁴

In performing quantitative simulations, it is essential to obtain precise relations between the calculation parameters in the equations and the real physical qualities. The asymptotic analysis can achieve this goal. Specifically, the perturbation analyses have been performed on each scale, including the inner scale (interface) and the outer scale (sharp-interface problem), then the two expansions are matched.³⁷ In this way, the calculation parameters in the PF equations and the physical qualities could be linked by:

$$d_0 = a_1 \frac{W}{\lambda} \quad (15)$$

$$\beta = a_1 \left(\frac{\tau}{\lambda W} - a_2 \frac{W}{D_L} \right) \quad (16)$$

In these equations, W and τ are the interface width and relaxation time, which are the length scale and time scale, respectively. $a_1=5\sqrt{2}/8$ and $a_2=47/75$. $d_0=\Gamma/|m|(1-k)(c_\infty/k)$ is the chemical capillary length, where $\Gamma=\gamma_{sl}T_f/(p_sL_f)$ is the Gibbs-Thomson coefficient, γ_{sl} is S/L interfacial energy, T_f is the melting point of pure solvent, and L_f is the latent heat. That is, [equation \(15\)](#) describes the Gibbs-Thomson effect, where λ is the coupling constant. [Equation \(16\)](#) expresses the relation between the kinetic coefficient β and other parameters. It contains two terms. The first term describes the dissipation due to a homogeneous undercooling of the interface. The second term represents the inhomogeneity of the temperature field inside the interface.³⁸ Due to the local equilibrium approximation, β is set to be zero in the simulations.

C. Computational procedure

In the computation, the material parameters of Al-2.0wt.%Cu are shown in [Table 1](#).^{39, 40}

When solving [equations \(2\)-\(4\)](#) numerically, for a small time interval Δt , the relations in [equations \(17\)-\(18\)](#) can be regarded as the initial conditions.⁸

$$l \approx \left(\frac{8D_L \cdot \Delta t}{3} \right)^{1/2} \quad (17)$$

$$z_0 = z_\infty - V_p(t) \cdot \Delta t + \frac{V_p(t) \sqrt{2D_L}}{\sqrt{3} \cdot z_\infty (1-k)} (\Delta t)^{3/2} \quad (18)$$

When solving [equation \(6\)](#), the dispersion relation, the increase rate σ_ω satisfies [equation\(19\)](#):⁸

$$\sigma_\omega = D_l \left(q_\omega^2 - \omega^2 \right) - q_\omega V_I \quad (19)$$

Setting $\sigma_\omega=0$, the solution of [equation \(19\)](#) is:

$$q_\omega = \frac{V_I}{2D_l} + \sqrt{\omega^2 + \left(\frac{V_I}{2D_l} \right)^2} \quad (20)$$

Eliminating q_ω from these equations and inserting the values of z_0 and l , the time-dependent spectrum of the increase rate $\sigma_\omega(t)$ can be obtained. Taking $\sigma_\omega(t)$ to [equation \(7\)](#), the time-dependent amplitude can be obtained. In [equation \(7\)](#), $A_\omega(0)$ reflects the initial amplitude. Based on the approximation of the equilibrium fluctuation spectrum, $A_\omega(0)$ equals the capillary length d_0 .³⁰

When solving the PF governing [equations \(9\)-\(10\)](#), the most important parameter is the interface width

W .¹⁹ The simulation accuracy increases as W decreases, while the computational cost increases dramatically as W decreases. Performing the thin interface limitation, the magnitude of W just needs to be one order of magnitude smaller than the characteristic length scale of the structure.^{31, 41} Since the characteristic length of alloy solidification is $L_C \sim \sqrt{d_0} * D_L / V_{tip}$,²⁷ W was set to be $0.15\mu\text{m}$. In the computation, the periodic boundary conditions were loaded for both the phase field and supersaturation field. The time step size was chosen below the threshold of numerical instability for the diffusion equations, i.e., $\Delta t < (\Delta x)^2 / (4D_L)$. Finally, when D_L is $3.0 \times 10^{-9}\text{m}^2/\text{s}$, this paper used fixed grid size $\Delta x = 0.8W$ and time step size $\Delta t = 0.013\tau$.

Moreover, a fluctuating current J_U is introduced to the diffusion equation to consider the infinitesimal perturbation of thermal noise on the S/L interface. By using the Euler explicit time scheme:

$$U^{t+\Delta t} = U^t + \Delta t \left(\partial_t U - \vec{\nabla} \cdot \vec{J}_U \right) \quad (21)$$

The components of J_U are random variables obeying a Gaussian distribution, which has the maximum entropy relative to other probability distributions:⁴²

$$\langle J_U^m(\vec{r}, t) J_U^n(\vec{r}', t') \rangle = 2D_L q(\phi) F_U^0 \delta_{mn} \delta(\vec{r} - \vec{r}') \delta(t - t') \quad (22)$$

In equation (22), the constant noise magnitude F_U^0 reflects the magnitude of F_U for a reference planar interface at temperature T_0 , defined as:^{25, 43}

$$F_U^0 = \frac{k v_0}{(1-k)^2 N_A c_\infty} \quad (23)$$

where v_0 is the molar volume of the solute atom, and N_A is the Avogadro constant. According to the Clausius-Clapeyron relation:

$$\frac{|m|}{1-k} = \frac{k_B T_0^2}{\Delta h} \quad (24)$$

where Δh is the latent heat, and k_B is the Boltzmann constant. The constant noise amplitude becomes:

$$F_U^0 = \frac{k}{|m| c_\infty (1-k)} \frac{k_B T_0^2}{L} \quad (25)$$

Finally, the program codes of the theoretical model and PF model were written in C++. The explicit Finite Difference Method (FDM) was used when solving the governing equations, and the Message Passing Interface (MPI) parallelization was adopted for improving the computational efficiency.

Table 1. The material parameters of Al-2.0wt.%Cu for simulations^{39, 40}

Symbol	Value	Unit
Liquidus temperature, T_L	927.8	K
Solidus temperature, T_S	896.8	K
Diffusion coefficient in liquid phase, D_L	3.0×10^{-9}	m^2/s
Equilibrium partition coefficient, k	0.14	/
Alloy composition, c_∞	2.0	wt.%
Liquidus slope, m	-2.6	K/wt.%
Gibbs-Thomson coefficient, Γ	2.4×10^{-7}	$\text{K} \cdot \text{m}$
Anisotropic strength of surface energy, ϵ_4	0.01	/

Results and discussion

In this section, varying solidification parameters are adopted in the simulations. The thermal gradient G is constant at 100K/mm, while the pulling speed V_P increases from 0 to a fixed value of 300μm/s, for which the increase time is 0.5s, shown in Fig. 1(a). The intersection angle between the TGD and PCO of the crystal is 30°. The domain of the PF simulation is 2400×2400 grids, corresponding to 288.0μm×288.0μm in the real unit. It takes about 30 hours using 40 cores to finish one job.

A. The dynamical evolution in a dissipative system

As mentioned before, by exchanging heat and mass with the environment, solidification patterns are dissipative structures formed out of equilibrium in an open system. The dissipative systems develop patterns or structures they do not have when first formed. Hence, the dynamical evolution of the characteristic parameters with time should be described clearly to represent the dissipative features better.

Fig. 1 shows the evolution of the characteristic parameters, including the concentration at interface c_0 and the instantaneous velocity of interface V_I . In Fig. 1(a), the curves from the WL model and PF model show good consistencies before the crossover time ($t=0.67\text{s}$) of the planar instability, validating the accuracy of the PF model. After the crossover time, the curves from the WL model and PF model differ from each other. Since the parameters obtained from the WL model are based on the planar interface, after the planar instability, the interfacial morphologies lead to the differences between these two models. That is, the differences do not mean the contradictions between these two models. Since the PF model can represent

complex interfacial morphologies, the following discussion of the characteristic parameters at the interface is based on the PF results.

Meanwhile, the sharp interface model of alloy solidification could describe the evolution of c_0 and V_I qualitatively and describe their features intuitively. Equations (26)-(27) express the one-sided sharp interface model of alloy solidification, where κ is the interfacial curvature and \dot{T} is the cooling rate ($=G*V_P$). $\partial_n c^+$ is the gradient of concentration at the liquid side of the interface. Since $\partial_n c^+ < 0$ in equations (27), to make the discussion intuitive, we set $|\partial_n c| = |\partial_n c^+|$.

$$c_0 = \frac{c_\infty}{k} - \frac{\kappa \cdot \Gamma + G(z - V_P t)}{|m|} = \frac{c_\infty}{k} - \frac{\kappa \cdot \Gamma + Gz + \dot{T}t}{|m|} \quad (26)$$

$$V_I = (-D_L \cdot \partial_n c^+) / [(1-k)c_0] = D_L \cdot |\partial_n c| / [(1-k)c_0] \quad (27)$$

According to the PF results and the sharp interface model, the dynamical evolution during directional solidification is the following. Fig. 1 shows the evolution of concentration c_0 and velocity V_I during the entire solidification process. The corresponding morphological evolution at the different stages is shown in Fig. 2. At the initial stage, in Fig. 1(a1), both c_0 and V_I increase. As time goes on, they reach the peaks and then decrease, shown in Fig. 1(a2). Through a period of oscillation, they turn into a steady state, shown in Fig. 1(a3). The detailed evolution at each stage is following:

At the planar growth stage, the accumulation of solute ahead of the interface makes c_0 increase. At this stage, the interfacial curvature is zero. As expressed in equation (26), both V_P and t increase with time. Hence, c_0 increases with time exponentially. Meanwhile, the increase of c_0 means $|\partial_n c|$ increases, in equation (27), making V_I increase with time. The evolution of c_0 and V_I at the planar growth stage is shown in Fig. 1(a1) and the corresponding morphological evolution is shown in Fig. 2(a).

As solidification goes on, the planar instability occurs, represented by the sharp increment of the V_I curves in Fig. 1(a1) and (a2). The morphological evolution is shown in Fig. 2(a). On the one hand, when instability occurs, due to mass conservation, the concentration c_0 still increases after the crossover time. On the other hand, the cellular appear after the instability. Due to the curvature of the cellular, rather than diffusing only along the pulling direction of the planar interface, the solute can diffuse along multiple directions from the cellular tip to the liquid, resulting in the decrease of c_0 (see equation (26)). That is, after the planar instability, the concentration ahead of the interface first increases and then decreases, shown by the limited increment of the c_0 curve after the crossover time in Fig. 1(a2). For the velocity V_I , equation (27)

shows the competitive influences of $|\partial_n c|$ and c_0 depend on their specific values. $|\partial_n c|$ is determined by V_I (by adjusting the diffusion length) and c_0 (by adjusting the difference between c_0 and c_∞), synergistically. It is evident that $|\partial_n c|$ has positive relations with both V_I and c_0 . After the planar instability, the increment of c_0 is very limited. By contrast, due to the increase of c_0 and the curvature of the cellular, the $|\partial_n c|$ increase greatly. Hence, the velocity V_I increases greatly, shown by the sharp increment of the V_I curve after the crossover time in Fig. 1(a2). After the peak of the c_0 curve, c_0 starts to decrease, and the velocity V_I increase further (see equation (27)). As time goes on, the further decrease of c_0 makes $|\partial_n c|$ decrease. As a result, V_I reaches the maximum value and then decreases. With the decrease of V_I , the interfacial curvature κ decreases, making c_0 increase (see equation (26)). The increase of c_0 brings the increase of $|\partial_n c|$, making the velocity V_I increase again. Then the increase of V_I brings the increase of κ , making c_0 decrease again. The cycle goes on and on till the steady-state stage, shown by the oscillating curves (from $t=1.0$ s to $t=2.2$ s) in Fig. 1(a2) and the morphological evolution in Fig. 2(b)-(c).

As time goes further, solidification turns into steady-state growth, shown by the stable curves (after $t=2.2$ s) in Fig. 1(a3) and the morphological evolution in Fig. 2(d). At this stage, the dissipative solidification structures achieve a quasi-steady state after a period of self-organization. Hence, both c_0 and V_I turn into a steady state.

In conclusion, the consistencies at the planar stage between the WL model and PF model demonstrate the accuracy of the PF simulations. After the planar instability, the interfacial effects make the evolution of concentration c_0 and tip velocity V_I complex. As time goes on, c_0 and V_I reach the peaks successively and then decrease. Subsequently, both the c_0 curve and V_I curve show oscillatory behaviors. Finally, they turn into a steady state. The evolitional characteristics of these parameters illustrate the dissipative features during directional solidification.

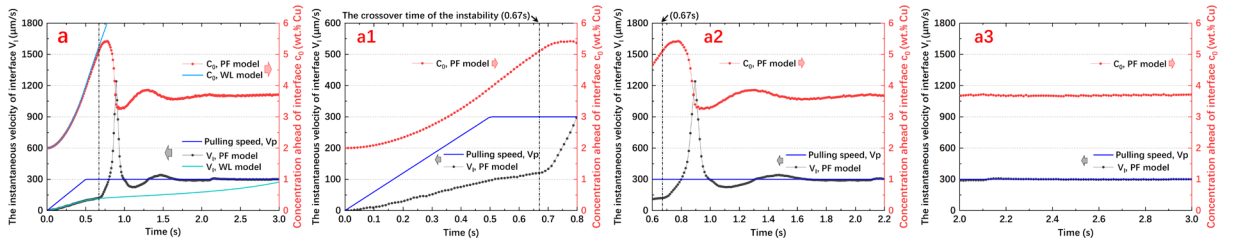


Fig. 1. The evolution of the characteristic parameters with time during the entire directional solidification: (a) the concentration ahead of the interface c_0 and the instantaneous velocity of the interface V_I ; (a1), (a2), and (a3) are the enlarged versions of (a).

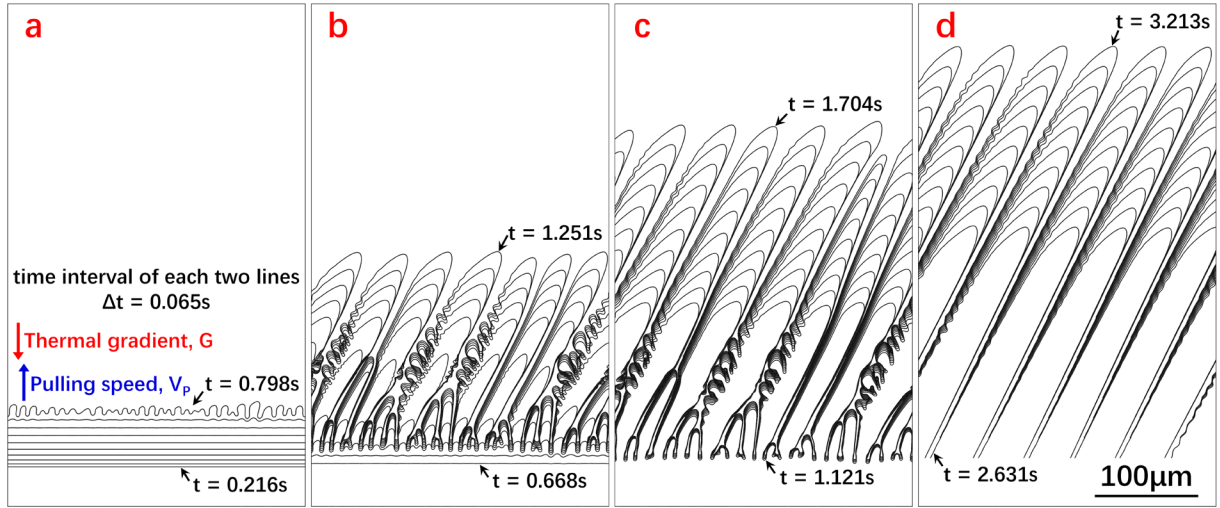


Fig. 2. The morphological evolution at different stages of the directional solidification: (a) the planar growth and instability; (b)-(c) the planar-to-cellular and dendrite growth (oscillation); (d) the steady-state growth.

B. The role of solute diffusion in a dissipative system

The previous section describes the dissipative features of solidification. The cause of dissipation and the factors affecting dissipation should be affirmed. According to statistical mechanics, dissipation results from the friction of atoms or molecules. Friction (dissipation) means the tendency of systems to move toward equilibrium when different degrees of freedom are allowed to interact with each other. For alloy solidification, dissipation is the tendency of supersaturation to equilibrium. The diffusion coefficient D_L and dissipation satisfy the relation:

$$D_L = \frac{k_B T}{\gamma_0} \quad (28)$$

where γ_0 is the friction coefficient (dissipation). Equation (28) illustrates the coefficient D_L has a negative relation with the degree of dissipation. That is, by adjusting the value of D_L , the dissipation of the system can be altered.

In this section, to represent different degrees of dissipation, different diffusion coefficients D_L are used in the PF simulations. D_L are set to be 2.0×10^{-9} , 3.0×10^{-9} , 4.0×10^{-9} and 6.0×10^{-9} m²/s, respectively. It should be noted, the variation of D_L here is just for parametric study, aiming to reveal the role of solute diffusion in morphological evolution. In the real physical world, D_L cannot vary within such a great range.

With different D_L , the evolution of the concentration at the interface c_0 and tip velocity V_I is shown in Fig. 3. On the one hand, the tendencies of c_0 and V_I curves show similar characteristics, including the sharp increments of the V_I curves, the peaks of the c_0 and V_I curves, the oscillation of the curves, and the stable

state of the curves. On the other hand, due to the different D_L , the degrees of dissipation are different during the evolution. Hence, the quantitative features of the evolution show differences, as follows.

1. The planar growth and instability

At the planar growth stage, the accumulation of solute ahead of the interface makes c_0 increase. At the same moment before the planar instability, in Fig. 3(a1), c_0 decreases from 2.0×10^{-9} to 6.0×10^{-9} . For the velocity V_I , according to equation (27), V_I has a positive relation with D_L while having a negative relation with c_0 . The larger D_L and smaller c_0 correspond to the larger V_I . At the same moment before the instability, V_I increases from 2.0×10^{-9} to 6.0×10^{-9} , shown in Fig. 3(b1).

As solidification goes on, the planar instability appears, represented by the sharp increments of the V_I curves in Fig. 3(b1)-(b2). To validate the PF results, the calculations of the theoretical model are performed, using the same parameters. By solving equations (5)-(7), the increase rate σ_ω and perturbation amplitude A_ω can be obtained, shown in Fig. 4. The time when σ_ω becomes positive represents the critical time of the marginal stability, shown by the red curves in Fig. 4(a1)-(a4). It should be noted, the critical time t_c here reflects the time that the perturbations can be amplified. At this moment, the perturbations at the interface are still infinitesimal, which cannot be observed at the mesoscale. Hence, rather than the time when σ_ω turns positive, we define the crossover time based on a specific value of A_ω . The time when the magnitude of A_ω reaches about $1\mu\text{m}$ is identified as the crossover time of the planar instability, shown by the purple curves in Fig. 4(b1)-(b4). Finally, the crossover times from the theoretical model are 0.63s, 0.67s, 0.69s, and 0.75s in Fig. 4, consisting of those from the PF simulations, 0.65s, 0.67s, 0.69s, and 0.76s in Fig. 3.

The consistencies between the two different models validate the accuracy of the simulations. Fig. 3 shows the crossover times of planar instability increase from 2.0×10^{-9} to 6.0×10^{-9} . Meanwhile, the onset of the instability corresponds to different V_I , illustrating the velocity V_I is not the criterion of the instability. On the other hand, the onset of the instability corresponds to similar c_0 . The results demonstrate the conclusion that the excess free energy at the interface and corresponding interfacial energy are the critical parameters of the instability.⁴⁴ Snapshots of the solute distribution at the crossover time are shown in Fig. 5(a1)-(a4). The larger D_L corresponds to the larger diffusion length ahead of the interface, while the concentration ahead of the interface (c_0) is almost the same with different D_L .

The detailed evolution of the interfacial morphologies with different D_L is shown in Fig. 5(b1)-(b4), where the time intervals between each two lines are the same ($\Delta t=0.043\text{s}$). On the one hand, the consuming

time of the Planar-Cellular-Transition (PCT) increases from 2.0×10^{-9} to 6.0×10^{-9} . Here the completion of the PCT is defined as the amplitude of the cellular becomes roughly comparable to its wavelength. On the other hand, the wavenumber of the cellular decreases from 2.0×10^{-9} to 6.0×10^{-9} .

According to [equation \(28\)](#), the coefficient D_L has a negative relation with the degree of dissipation. The smaller D_L means the larger degree of dissipation. Hence, the consuming time of the PCT increases from 2.0×10^{-9} to 6.0×10^{-9} , shown in [Fig. 5\(b1\)-\(b4\)](#). Meanwhile, the solute atoms still accumulate at the interface during the PCT, till the appearing of the cellular. The longer time of the PCT means the longer time of solute accumulation. Hence, the peak of c_0 appears later and later from 2.0×10^{-9} to 6.0×10^{-9} , in [Fig. 3\(a2\)](#), and the values of the peak increase from 2.0×10^{-9} to 6.0×10^{-9} . For the velocity V_I , the larger D_L means the lower degree of dissipation and the smaller V_I . In [Fig. 3\(b2\)](#), during the PCT stage, V_I decreases from 2.0×10^{-9} to 6.0×10^{-9} . The decreasing V_I makes the interfacial curvature κ decrease from 2.0×10^{-9} to 6.0×10^{-9} . The smaller κ means the larger wavelength and smaller wavenumber, i.e., the wavelength of the cellular increases from 2.0×10^{-9} to 6.0×10^{-9} while the wavenumber decreases, shown in [Fig. 5\(b1\)-\(b4\)](#).

In conclusion, at the planar growth stage, the larger D_L corresponds to the smaller c_0 and the larger V_I . Different V_I at the crossover times of planar instability illustrate the velocity V_I is not the criterion of the instability. The decrease of the interfacial energy, induced by solute segregation at the S/L interface, can be regarded as the criterion of instability. During the PCT stage, the larger D_L means the smaller degree of dissipation. As a result, the consuming time of the PCT increases from 2.0×10^{-9} to 6.0×10^{-9} , while the tip velocity V_I and the interfacial curvature κ decreases from 2.0×10^{-9} to 6.0×10^{-9} . Correspondingly, the wavelength of the cellular increases from 2.0×10^{-9} to 6.0×10^{-9} while the wavenumber decreases.

2. The dendrite growth

After the planar instability and the PCT stage, the dendrites (formed from the cellular) start to grow. At this stage, according to the rule of maximum surface energy, the crystal will seek to minimize the total energy by creating large curvature in the $<100>$ direction, shown in [Fig. 6\(b1\)-\(b4\)](#). On the other hand, different D_L make the evolutional characteristics differ from each other, including the concentration c_0 and tip velocity V_I in [Fig. 3\(a2\)-\(b2\)](#), as well as the interfacial morphologies in [Fig. 6](#).

After the appearing of the cellular, c_0 starts to decrease. As mentioned before, the tip curvature κ and velocity V_I decreases from 2.0×10^{-9} to 6.0×10^{-9} . Correspondingly, the gradient $|\partial_n c|$ decreases from 2.0×10^{-9} to 6.0×10^{-9} . Combined with [equation \(27\)](#), V_I increases further and reaches its peak. The smaller D_L

corresponds to the larger κ , the smaller c_0 , and the larger $|\partial_n c|$. Hence, the peak values of V_I decrease from 2.0×10^{-9} to 6.0×10^{-9} , shown in Fig. 3(b2). Meanwhile, the smaller D_L means the larger degree of dissipation and non-equilibrium, leading to more non-equilibrium structures (sidebranches), shown in Fig. 6(b1)-(b4).

It should be noted, in Fig. 6 (a1)-(a4), the solute diffusion ahead of the interface is dominated by the magnitude of D_L , represented by the increasing diffusion length and the decreasing gradient of concentration from 2.0×10^{-9} to 6.0×10^{-9} . By contrast, the solute diffusion between the dendrite trunks is affected by D_L as well as the interfacial curvature, i.e., curvature-induced solute diffusion. During the directional solidification, due to the constrained growth conditions, the overall solute distribution is determined by the temperature. Hence, the gradients of solute concentration between the dendrite trunks show the same features.

In conclusion, the dendrites with smaller D_L grow out more sidebranches. On the other hand, different D_L makes the gradients of solute concentration ahead of the interface decrease from 2.0×10^{-9} to 6.0×10^{-9} , while the gradients of concentration between the dendrite trunks show the same features.

3. The steady-state growth

As time goes further, solidification turns into the steady-state growth stage, shown by the stable curves in Fig. 3(a3)-(b3) and the morphological evolution in Fig. 7. At this stage, the dissipative solidification structures achieve a quasi-steady state after a period of self-organization. With different D_L , the overall propagation velocities of the S/L interface are the same and equal to the pulling speed V_P , shown in Fig. 3(b3). By contrast, due to the different D_L , the concentration at the interface c_0 decreases from 2.0×10^{-9} to 6.0×10^{-9} , shown in Fig. 3(a3). In Fig. 7(a1)-(a4), on the one hand, the gradients of concentration ahead of the interface decrease from 2.0×10^{-9} to 6.0×10^{-9} . On the other hand, under the constrained growth conditions of directional solidification, the overall distribution of solute distribution is determined by the temperature. The gradients of concentration between the dendrite trunks show the same features.

The morphological characteristics include the primary dendrite and sidebranches, determined by the primary dendrite arm space.⁴⁵ In Fig. 7, the space increases from 2.0×10^{-9} to 6.0×10^{-9} , consisting of the rule of length scale selection, in equation (29), qualitatively.⁴⁶

$$\rho = \frac{1}{\sigma^*} \sqrt{d_0 \frac{D_L}{V_I}} \quad (29)$$

where σ^* is the selection constant, motivated by the value obtained for the minimum wavelength found in the stability analysis of planar growth. The larger D_L corresponds to the larger tip radius ρ , the larger arm space,

and the smaller number of primary dendrites.

The onset of sidebranches needs the primary arm space is greater than one critical value. Hence, we focus on [Fig. 7\(b3\) and \(b4\)](#) here, whose space is large enough. With the same primary space and tip velocity, the dendrites with smaller D_L grow out more sidebranches. The result consists of the previous conclusion. The smaller D_L means the larger degree of dissipation and non-equilibrium. Hence, more non-equilibrium structures (sidebranches) grow out.

To represent this phenomenon more clearly, the simulations with a given number of primary dendrites are performed. With different D_L and the same number of primary dendrites, the steady-state growth is shown in [Fig. 8](#). Although with the same primary dendrite arm space λ_1 and tip velocity V_I , the dendrites have different tip curvature κ . Specifically, κ decreases from 2.0×10^{-9} to 6.0×10^{-9} . In addition, with the same λ_1 and V_I , the evolution of sidebranches shows differences. [Fig. 8](#) shows both the number and amplitude of the sidebranches decrease from 2.0×10^{-9} to 6.0×10^{-9} . The smaller D_L means the larger degree of dissipation and non-equilibrium. Hence, even with the same λ_1 and V_I , the curvature κ and the number and amplitude of the sidebranches decrease from 2.0×10^{-9} to 6.0×10^{-9} .

The phenomena reveal the following things. (1) With the same solidification parameters and material parameters, in [Fig. 7](#) and [Fig. 8](#), the evolution of solidification is quite different due to their different initial conditions. It consists of the fact that the initial conditions are deterministic for the following evolution in a dissipative system. (2) Comparing the evolution with different D_L in [Fig. 8](#), the interfacial morphologies do not have unique relations with the characteristic parameters. Due to different degrees of dissipation, even with the same arm space and tip velocity, the tip curvatures and the features of sidebranches are different.

In conclusion, at the steady-state stage, with different D_L , the overall propagation velocities of the S/L interface are the same and equal V_p . On the other hand, different D_L means different degrees of dissipation. Although with the same tip velocity and primary arm space, the dendrites with different D_L have different tip curvatures and different features of sidebranches.

The investigations in this paper indicate the importance of solute diffusion in alloy solidification. The dissipation at the interface is altered by the diffusion coefficient D_L . From the viewpoint of the whole domain, smaller D_L corresponds to a higher degree of dissipation of the system, as well as more exchange of heat and mass with the environment. Hence, more S/L interfaces are formed during solidification. The areas of the interfaces decrease from 2.0×10^{-9} to 6.0×10^{-9} , shown in [Fig. 5\(b1\)-\(b4\)](#), [Fig. 6\(b1\)-\(b4\)](#), [Fig. 7 \(b1\)-\(b4\)](#), and

Fig. 8 (b1)-(b4).

In addition, the investigations explain the conclusion that the competitive influences of curvature and velocity depend strongly on the ratio τ/W^2 in the governing equations.¹⁸ In the current PF model, based on the expression of the kinetic coefficient β in equation (16) and the local equilibrium approximation ($\beta=0$), one can obtain the relation:

$$\frac{\tau}{W^2} = a_2 \frac{\lambda}{D_L} \quad (30)$$

According to equations (30) and (15), we know that d_0 , a_1 , a_2 , W , and λ are constant during the PF simulation. Hence, the ratio τ/W^2 is dominated by the diffusion coefficient D_L . Meanwhile, D_L directly corresponds to the dissipation of the system. That is, the competitive influences of curvature and velocity (the ratio τ/W^2) are because of the dissipation, resulting from the friction of atoms.

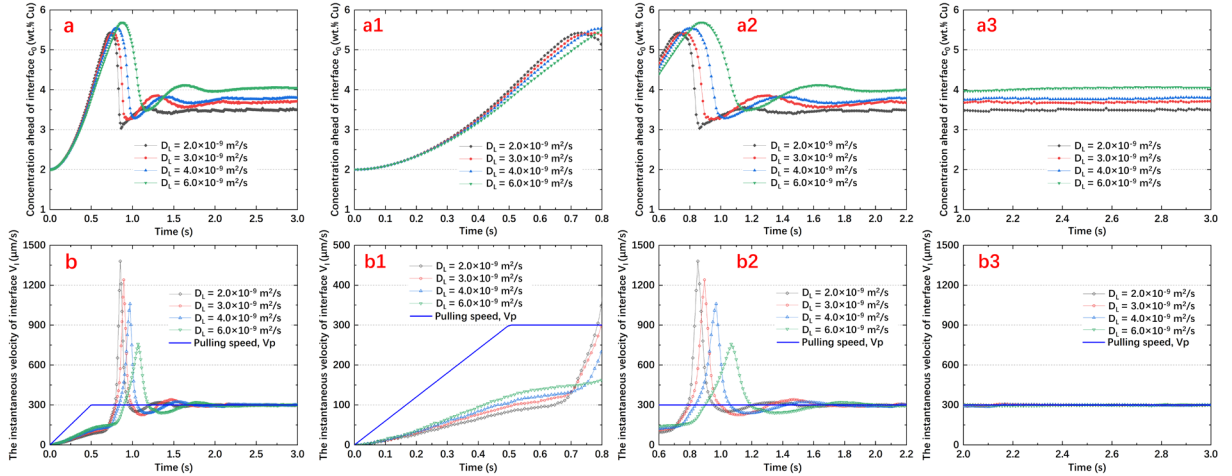


Fig. 3. The evolution of characteristic parameters with different diffusion coefficients D_L : (a) the concentration c_0 and (b) the instantaneous velocity V_i ; (a1), (a2), and (a3) are the enlarged versions of (a); (b1), (b2), and (b3) are the enlarged versions of (b). (from the PF simulations)

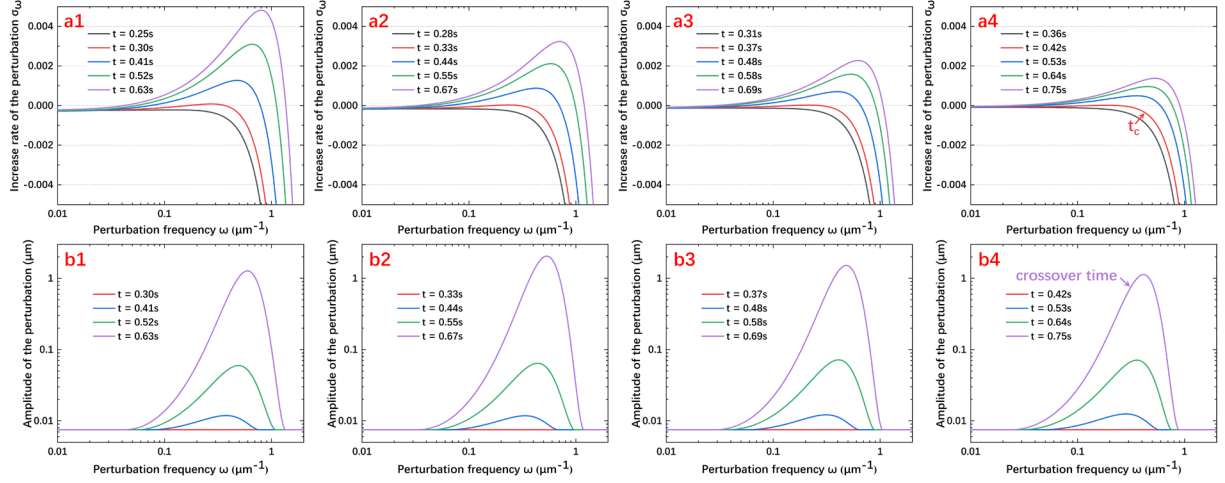


Fig. 4. Dynamical evolution of the instability predicted by the theoretical model with different solute diffusion coefficients D_L : (a) The increase rate of amplitude spectrum, (b) The evolution of the amplitude spectrum. (the diffusion coefficients are $2.0, 3.0, 4.0$, and $6.0 \times 10^{-9} \text{ m}^2/\text{s}$, respectively)

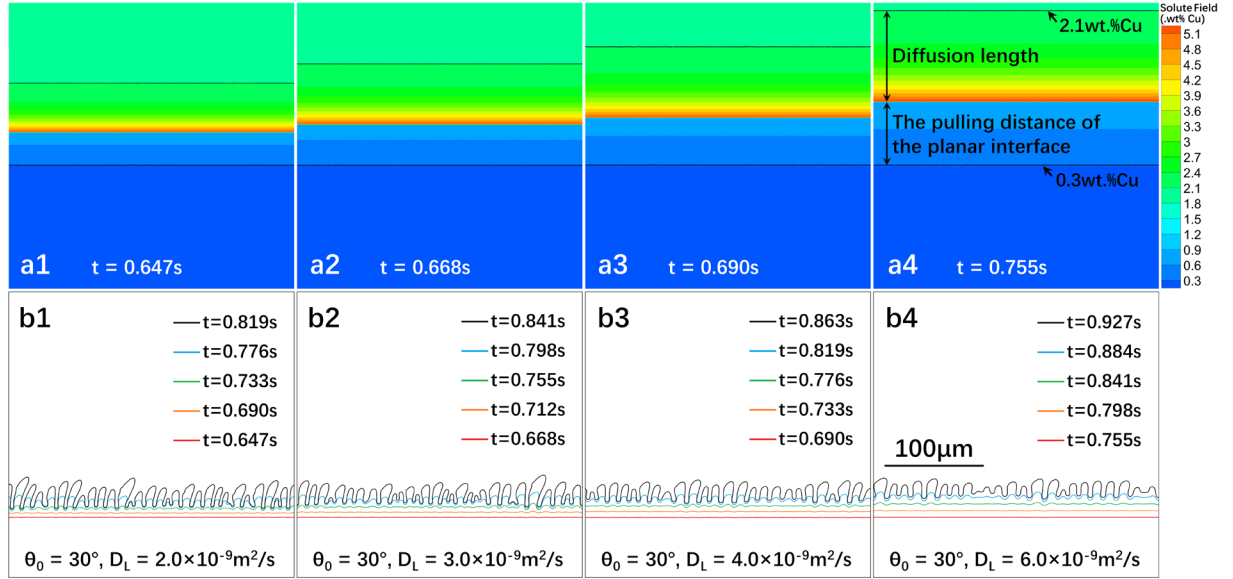


Fig. 5. (a) The solute distribution with different diffusion coefficient D_L at the onset time of the planar instability; (b) the corresponding evolution of the interfacial morphologies with different D_L at the Planar-Cellular-Transition stage. (from the PF simulations)

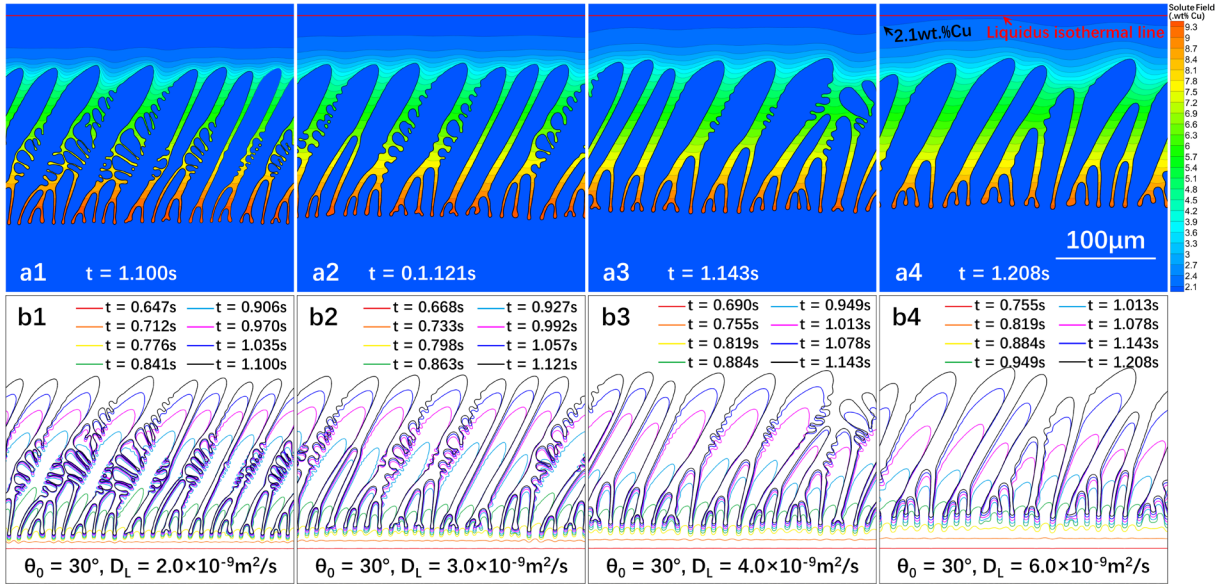


Fig. 6. (a) The solute distribution with different diffusion coefficient D_L at the dendrite growth stage; (b) the corresponding evolution of the interfacial morphologies with different D_L at this stage. (from the PF simulations)

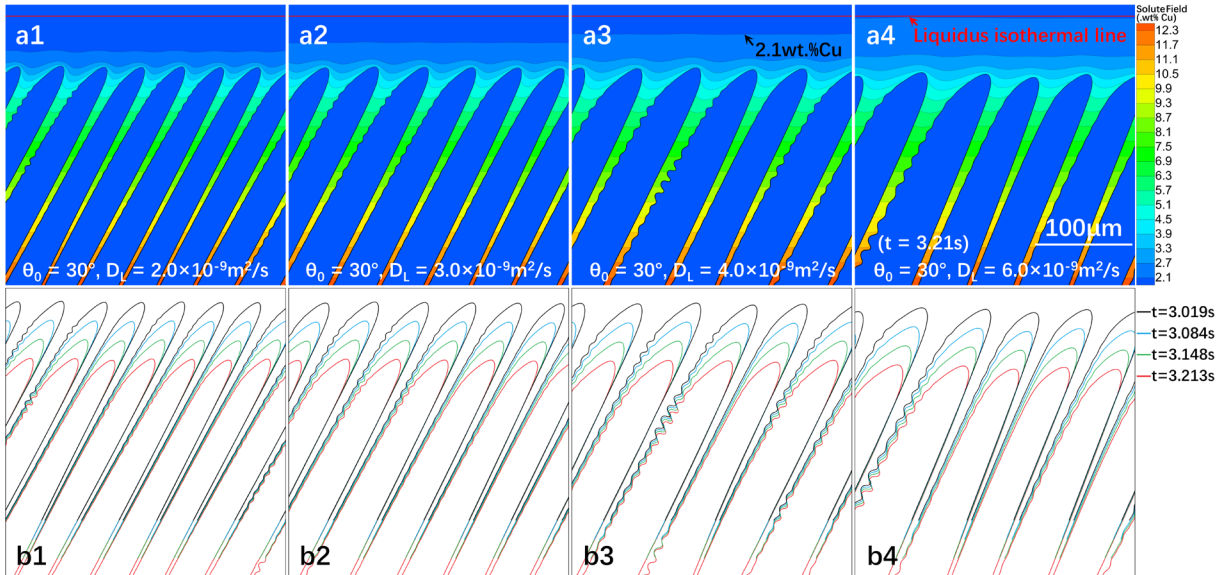


Fig. 7. (a) The solute distribution with different diffusion coefficient D_L at the steady-state stage ($t=3.21s$); (b) the corresponding evolution of the interfacial morphologies with different D_L at this stage. (from the PF simulations)

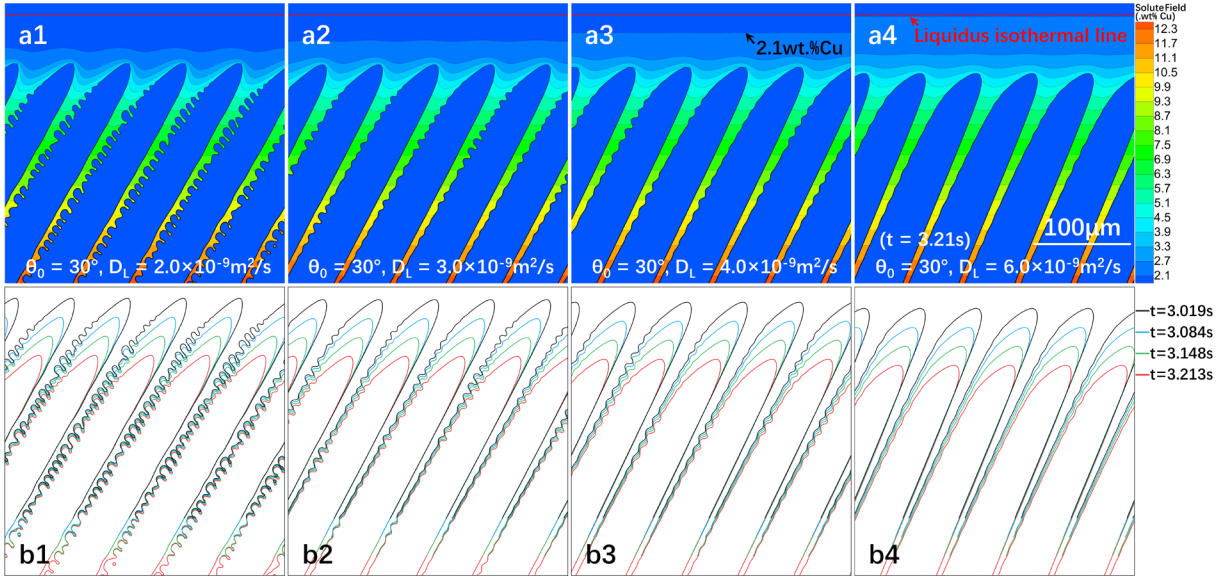


Fig. 8. (a) The solute distribution with the given number of dendrites and different diffusion coefficient D_L at the steady-state stage ($t=3.21\text{s}$); (b) the corresponding evolution of the interfacial morphologies at this stage. (from the PF simulations)

Summary

Through the quantitative PF model, this paper investigates the evolution in the whole domain during entire directional solidification. Firstly, the evolution of the characteristic parameters is discussed in detail. Secondly, by adjusting the coefficient D_L , the dissipation at the interface can be altered. With different D_L , different stages during directional solidification are investigated, including planar growth and instability, dendrite growth, and steady-state growth. The following conclusions can be drawn from the study:

- (1) The consistencies at the planar stage between the WL model and PF model demonstrate the accuracy of the PF simulations. After the planar instability, the interfacial effects make the evolution of concentration at interface c_0 and tip velocity V_I complex. The evolutional characteristics of the parameters show dissipative features.
- (2) At the planar growth stage, the larger D_L corresponds to the smaller c_0 and the larger V_I . Different V_I at the crossover times of planar instability illustrate the velocity V_I is not the criterion of the instability. The decrease of the interfacial energy, induced by solute segregation at the S/L interface, can be regarded as the criterion of instability. During the PCT stage, the larger D_L means the smaller degree of dissipation. Hence, the consuming time of the PCT increases from 2.0×10^{-9} to 6.0×10^{-9} while the tip velocity V_I and the interfacial curvature κ decreases. Correspondingly, the wavelength of the cellular increases from 2.0×10^{-9} to 6.0×10^{-9} while the wavenumber decreases.

(3) At the dendrite growth stage, dendrites with smaller D_L grow out more sidebranches. On the other hand, different D_L makes the gradients of solute concentration ahead of the interface decrease from 2.0×10^{-9} to 6.0×10^{-9} , while the gradients of concentration between the dendrite trunks show the same features.

(4) At the steady-state stage, with different D_L , the overall propagation velocities of the S/L interface are the same and equal V_p . On the other hand, different D_L means different degrees of dissipation. Although with the same tip velocity and primary arm space, the dendrites with different D_L have different tip curvatures and different features of sidebranches.

The investigations indicate the important role of solute diffusion in alloy solidification. The dissipation at the interface is altered by the diffusion coefficient D_L . From the viewpoint of the whole domain, smaller D_L corresponds to a higher degree of dissipation, as well as more exchange of heat and mass with the environment. Hence, more S/L interfaces are formed during solidification.

In addition, the investigations explain the conclusion that the competitive influences of curvature and velocity depend strongly on the ratio τ/W^2 . The ratio τ/W^2 is dominated by D_L , and D_L corresponds to the dissipation. Hence, the competitive influences of tip curvature and velocity are because of the dissipation, resulting from the friction of atoms.

Reference

1. W. Kurz, D.J. Fisher, R. Trivedi, *International Materials Reviews* **64**, 311 (2019).
2. J.J. Hoyt, M. Asta, T. Haxhimali, A. Karma, R.E. Napolitano, R. Trivedi, B.B. Laird, J.R. Morris, *MRS Bulletin* **29**, 935 (2004).
3. W. Kurz, M. Rappaz, R. Trivedi, *International Materials Reviews* **66**, 30 (2021).
4. J.T. McKeown, A.J. Clarke, J.M.K. Wiezorek, *MRS Bulletin* **45**, 916 (2020).
5. A. Karma, D. Tourret, *Current Opinion in Solid State and Materials Science* **20**, 25 (2016).
6. W.A. Tiller, K.A. Jackson, J.W. Rutter, B. Chalmers, *Acta Metallurgica* **1**, 428 (1953).
7. W.W. Mullins, R.F. Sekerka, *Journal of Applied Physics* **35**, 444 (1964).
8. J.A. Warren, J.S. Langer, *Physical Review E* **47**, 2702 (1993).
9. Y. Chen, A.-A. Bogno, N.M. Xiao, B. Billia, X.H. Kang, H. Nguyen-Thi, X.H. Luo, D.Z. Li, *Acta Materialia* **60**, 199 (2012).
10. W. Losert, B.Q. Shi, H.Z. Cummins, *Proceedings of the National Academy of Sciences* **95**, 431 (1998).
11. M. Ben Amar, E. Brener, *Physical Review Letters* **71**, 589 (1993).
12. E. Brener, *Physical Review Letters* **71**, 3653 (1993).
13. M.A. Jaafar, D.R. Rousse, S. Gibout, J.-P. Bédécarrats, *Renewable and Sustainable Energy Reviews* **74**, 1064 (2017).
14. M. Asta, C. Beckermann, A. Karma, W. Kurz, R. Napolitano, M. Plapp, G. Purdy, M. Rappaz, R. Trivedi, *Acta Materialia* **57**, 941 (2009).
15. D. Tourret, H. Liu, J. Llorca, *Progress in Materials Science* **123**, 100810 (2022).
16. L.-Q. Chen, Y. Zhao, *Progress in Materials Science* **124**, 100868 (2022).
17. D. Kammer, P.W. Voorhees, *MRS Bulletin* **33**, 603 (2008).
18. G. Caginalp, *Annals of Physics* **172**, 136 (1986).
19. A. Karma, W.-J. Rappel, *Physical Review E* **57**, 4323 (1998).

20. F. Yu, Y. Wei, *Metallurgical and Materials Transactions A* **49**, 3293 (2018).
21. Z. Dong, W. Zheng, Y. Wei, K. Song, *Physical Review E* **89** (2014).
22. L. Wang, Y. Wei, *JOM* **70**, 733 (2018).
23. H. Xing, K. Ankit, X. Dong, H. Chen, K. Jin, *International Journal of Heat and Mass Transfer* **117**, 1107 (2018).
24. W. Zheng, Z. Dong, Y. Wei, Y. Wang, *Crystal Research and Technology* **49**, 777 (2014).
25. B. Echebarria, A. Karma, S. Gurevich, *Physical Review E* **81**, 021608 (2010).
26. L.M. Pismen: Patterns and interfaces in dissipative dynamics, (Springer-Verlag, Heidelberg, Germany, 2006).
27. J.A. Dantzig, M. Rappaz: Solidification: 2nd Edition - Revised & Expanded, (EPFL Press, Lausanne, Switzerland, 2016).
28. F. Yu, Y. Wei, *Computational Materials Science* **169**, 109128 (2019).
29. Z. Wang, J. Wang, G. Yang, *Physical Review E* **80** (2009).
30. Z. Wang, J. Wang, G. Yang, *Applied Physics Letters* **94** (2009).
31. B. Echebarria, R. Folch, A. Karma, M. Plapp, *Physical Review E* **70**, 061604 (2004).
32. N. Provatas, T. Pinomaa, N. Ofori-Opoku: Quantitative Phase Field Modelling of Solidification, (CRC Press, Boca Raton, FL, 2021).
33. R.F. Sekerka: 5 - Open Systems, in Thermal Physics (Elsevier, Amsterdam, 2015), pp. 53.
34. A. Karma, *Physical Review Letters* **87**, 115701 (2001).
35. S. Gurevich, M. Amoorezaei, N. Provatas, *Physical Review E* **82**, 051606 (2010).
36. G. Caginalp, *Archive for Rational Mechanics and Analysis* **92**, 205 (1986).
37. M. Plapp, *Journal of the Indian Institute of Science* **96**, 179 (2016).
38. M. Plapp: 15 - Phase-Field Models, in Handbook of Crystal Growth (Second Edition), edited by T. Nishinaga (Elsevier, Boston, 2015), pp. 631.
39. A.J. Clarke, D. Tourret, Y. Song, S.D. Imhoff, P.J. Gibbs, J.W. Gibbs, K. Fezzaa, A. Karma, *Acta Materialia* **129**, 203 (2017).
40. J.R. Morris, *Physical Review B* **66**, 144104 (2002).
41. H. Xing, X. Dong, H. Wu, G. Hao, J. Wang, C. Chen, K. Jin, *Scientific Reports* **6**, 26625 (2016).
42. A. Karma, W.-J. Rappel, *Physical Review E* **60**, 3614 (1999).
43. F. Yu, Y. Ji, Y. Wei, L.-Q. Chen, *International Journal of Heat and Mass Transfer* **130**, 204 (2019).
44. F. Yu, *arXiv preprint arXiv:2210.15123* (2022).
45. H. Xing, X.L. Dong, C.L. Chen, J.Y. Wang, L.F. Du, K.X. Jin, *International Journal of Heat and Mass Transfer* **90**, 911 (2015).
46. H. Müller-Krumbhaar, J.S. Langer, *Acta Metallurgica* **26**, 1697 (1978).